Ultrasound-induced generation of multielectron bubbles in liquid helium

Neha Yadav [●],[1] Yunhu Huang,[2] and Ambarish Ghosh [●][1,2,*]

[1]*Department of Physics, Indian Institute of Science, Bangalore 560012, India*
[2]*Centre for Nano Science and Engineering, Indian Institute of Science, Bangalore 560012, India*

Multielectron bubbles provide a unique platform to study electrons in two dimensions and on curved surfaces, at densities which cannot be accessed using electrons on bulk helium or in semiconductor interfaces. Usually, MEBs are created by applying a large electric field and thereby inducing electrohydrodynamical instability on a charged surface of liquid helium. In the present study, we describe a method to create instability of the charged surface using ultrasound, in the presence of small electric fields. The ultrasound was applied close to the charged liquid-vapor interface, resulting in the formation of a liquid column, which breaks into liquid droplets. The mechanical impact of the droplets falling back into the bulk liquid resulted in the formation of highly charged multielectron bubbles. We estimated the initial charge density of the bubbles above the lambda point to be close to 10^{13} electrons/m^2.

I. INTRODUCTION

An electron approaching helium surface experiences a repulsive 1-eV potential [1] due to the Pauli exclusion principle. At the same time, the electron experiences a weak long-range electrostatic attraction due to the finite electrical polarizability of the liquid. This results in the formation of a two-dimensional electron system (2DES) above liquid helium, which is bound in the direction perpendicular to the liquid surface. The difference between electric field magnitudes above (E_u) and below (E_l) the surface is related to the number of electrons on the surface by the relation $E_u - E_l = ne/\varepsilon_0$, where n is the density of electrons on the surface and ϵ_0 is the absolute permittivity of free space. When the surface density n exceeds a critical electron density $n_c = 2 \times 10^{13}$ electrons/m^2, equivalent to electric field of $\sim$4 kV/cm applied [2] to the surface, an electrohydrodynamical (EHD) instability develops. This instability results in a local nonuniform distribution of the electrons that can no longer be counteracted by the restoring forces (gravity and surface tension). This leads to the formation of multielectron bubbles (MEBs), which are cavities in the liquid containing many electrons. The energy of an MEB can be written as the sum of Coulomb energy between the electrons, energy due to curvature of the surface, and the thermodynamic work done to create the cavity. MEBs provide a promising platform to study interacting electrons on curved surfaces and allow electron densities to go beyond 2×10^{13} electrons/m^2 into the regime where quantum fluctuations of the 2DES can be significant [3–5].

Herein lies our motivation to create and observe MEBs with high electron density, which may even allow the observation of quantum melting if sufficiently high electron densities are reached. One must mention and compare with the 2DES in other solid-based systems [6], like Si-MOS or GaAs-AlGaAs

interfaces, which show strong quantum correlations and were found to be in the Fermi-liquid phase even at the minimum achieved electron densities. A more likely candidate to reach this goal is the system of charged thin films of helium [7], where the surface instabilities are suppressed so as to allow densities larger than n_c. This approach [8,9] is limited by the surface defects of the underlying substrate and loss of electrons sliding along quantized vortices; even so, there have been preliminary reports of electron densities reaching $\sim 10^{15}$ m^{-2} in the past [10]. However, so far there has been no definite experimental proof of the observation of a 2DES quantum melting transition, or signature of strong quantum correlations in a 2D electron solid in any of the systems mentioned above. MEBs may be able to bridge this gap in our current understanding of the phase diagram [5] of interacting electrons in two dimensions.

In equilibrium, the energy of an MEB can be written as follows:

$$E = \frac{Z^2 e^2}{8\pi \epsilon R} + \frac{4}{3}\pi R^3 P + 4\pi R^2 \alpha, \tag{1}$$

where R is the radius of the bubble, Z is the number of electrons, P is the pressure applied to the liquid, α is the surface tension coefficient of liquid helium, and $\epsilon = \varepsilon_0 \epsilon_r$ is the permittivity with ϵ_r being the relative permittivity ($\sim$1.057) of bulk helium. Note that this formula assumes the bubble size to be large enough to ignore certain energy contributions of the 2DES, e.g., that due to quantum confinement of the electron layer in a thin spherical shell as well as the electrons' exchange interactions. It is possible that the bubbles contain vapor, which below the lambda point will condense in the order of a few milliseconds because of the convective heat transport in superfluid helium; however, above the lambda point, vapor will condense slowly as the heat is carried away diffusively [11]. The equilibrium radius of the bubble can be

*ambarish@iisc.ac.in

written as

$$R_0 = \left(\frac{Z^2 e^2}{64\pi^2 \epsilon \alpha + 32\pi \epsilon P R_0} \right)^{1/3}. \quad (2)$$

For a bubble containing 10^5 electrons at $P = 0$, the equilibrium radius is $\sim 5\,\mu$m. The presence of vapor makes the bubble larger, which in turn helps stabilize the bubble against small shape fluctuations [12,13].

Experimentally MEBs were first observed by Volodin *et al.* [14]. They created the MEBs, or "bubblons," below the λ point by charging the surface using a tungsten filament and increasing the electric field above the critical value. Above the λ point, Albrecht *et al.* [15] used a similar technique to charge the surface and created the MEBs, and subsequently measured their charges. They also demonstrated that the bubbles formed are indeed charged and reacted to the change in electric field. Recently, Vadakkumbatt *et al.* [16] used confined field emission to create MEBs, trapped them using a Paul trap [17], and measured their charges and radii in a nondestructive manner. These experiments were carried out above T_λ, and the method of creation resulted in MEBs with a significant amount of vapor in them. The initial size of the MEBs was in the range of $10\text{--}100\,\mu$m and the number of electrons was in the order of $2000 - 10^4$, corresponding to initial charge densities $\sim 2\times10^{12}$ electrons/m^2. The vapor inside the MEBs condensed steadily [11] such that the electron density increased with time. However, before the densities were large enough for quantum correlations within the 2DES to be significant, the bubbles shrunk to sizes too small to be imaged.

In this paper, we report a technique of creating MEBs both above and below the λ point, of initial sizes similar to those from previous experiments, in the range of $10\text{--}100\,\mu$m. However, the typical numbers of electrons inside these MEBs were much larger, corresponding to initial charge densities as high as $n_c = 2\times10^{13}$ electrons/m^2. With gradual condensation of vapor [11] and corresponding reduction in the bubble sizes, we expect to achieve 2DES with strong quantum correlations, while the MEBs would still be observable with standard imaging systems.

II. EXPERIMENTAL SETUP

The experimental setup, shown schematically in Fig. 1, consisted of a nickel-63 radioactive foil to produce electrons to charge the helium surface. It was placed inside a brass housing that was connected to a voltage source. A voltage was applied to the ring below the brass housing to control the electric field above and across the liquid surface. The confinement cylinder consisted of four electrodes that were used to apply electric fields in the radial direction, with four 5 mm×6 mm openings in between them for imaging. A negative voltage between -200 and -500 V applied on this cylinder confined the electrons to the center of the charged interface. The hemispherical ultrasonic transducer was made of PZT-4 and resonated at 1 MHz, whose acoustic focus was approximately 0.75 mm above its top edge. For all the experiments reported here, the liquid level was kept at around 1 to 2 mm above the acoustic focus. It was also possible to vary the electric field in the bulk liquid by applying suitable
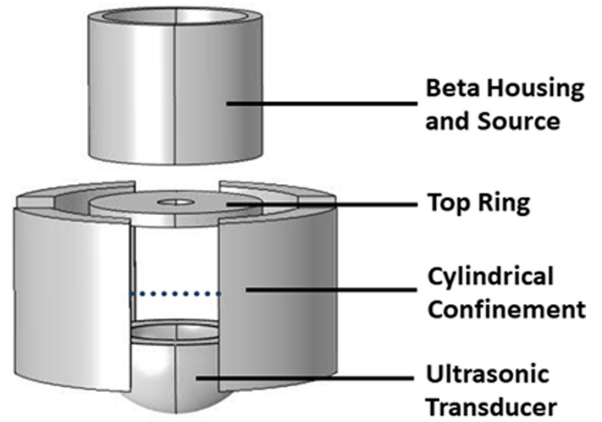

FIG. 1. The experimental setup used in the experiment. Ni-63 radioactive foil was placed within a housing made of brass. The top plate was used to control the electric field above and across the surface. The cylindrical confinement helped confine the electrons to the center of the charged surface. The level of liquid helium in the experimental setup is shown by the dashed blue line.

dc voltages to the inner conductive surface of the ultrasonic transducer. We used a highspeed camera (PHOTRON) for imaging the events at 10 000 frames per second.

III. EXPERIMENTAL OBSERVATIONS

As shown in the sequence of images in Fig. 2(a), beyond a critical ultrasound intensity, the liquid surface was deformed and pushed upwards by acoustic radiation pressure. The pulse width of the acoustic wave was $200\,\mu$s. Following the deformation of the helium surface, a spray of helium mist and droplets were ejected outward. After some time (~ 4 ms), the droplets coalesced together and formed a liquid column. This column continued to move up for some more time and then started to recede back towards the surface. This is shown in Fig. 2(b). During the descent back towards the surface, the column broke into millimeter-sized droplets. These droplets, as shown in Fig. 2(c), dropped and pushed down on the surface. Subsequently, the surface would either bounce back (not shown), or break and form an MEB, as shown in frames corresponding to 42.0–43.4 ms in Fig. 2(c). Note that there were also a few instances where the column did not break into droplets, yet MEBs were produced. The generation of MEBs appeared to be induced by mechanical impact on the charged interface. It is also worth mentioning that if the surface was uncharged, we did not see formation of any bubbles.

The formation of MEBs was found to depend on three parameters: duration of acoustic pulse, ac voltage applied to the transducer (V_{ac}), and voltages applied to the top ring. For example, for acoustic pulse width less than $50\,\mu$s, the surface deformation was not large enough. As a result, the liquid column was not formed, which was necessary for the formation of MEBs. We also investigated the effect of V_{ac} for pulse width of $200\,\mu$s for two voltages applied at the top ring. Note that V_{ac} was directly proportional to the amplitude of pressure oscillation in the liquid and therefore the ultrasonic radiation pressure. The probability of formation of at least one MEB is measured out of 50 trials, shown in
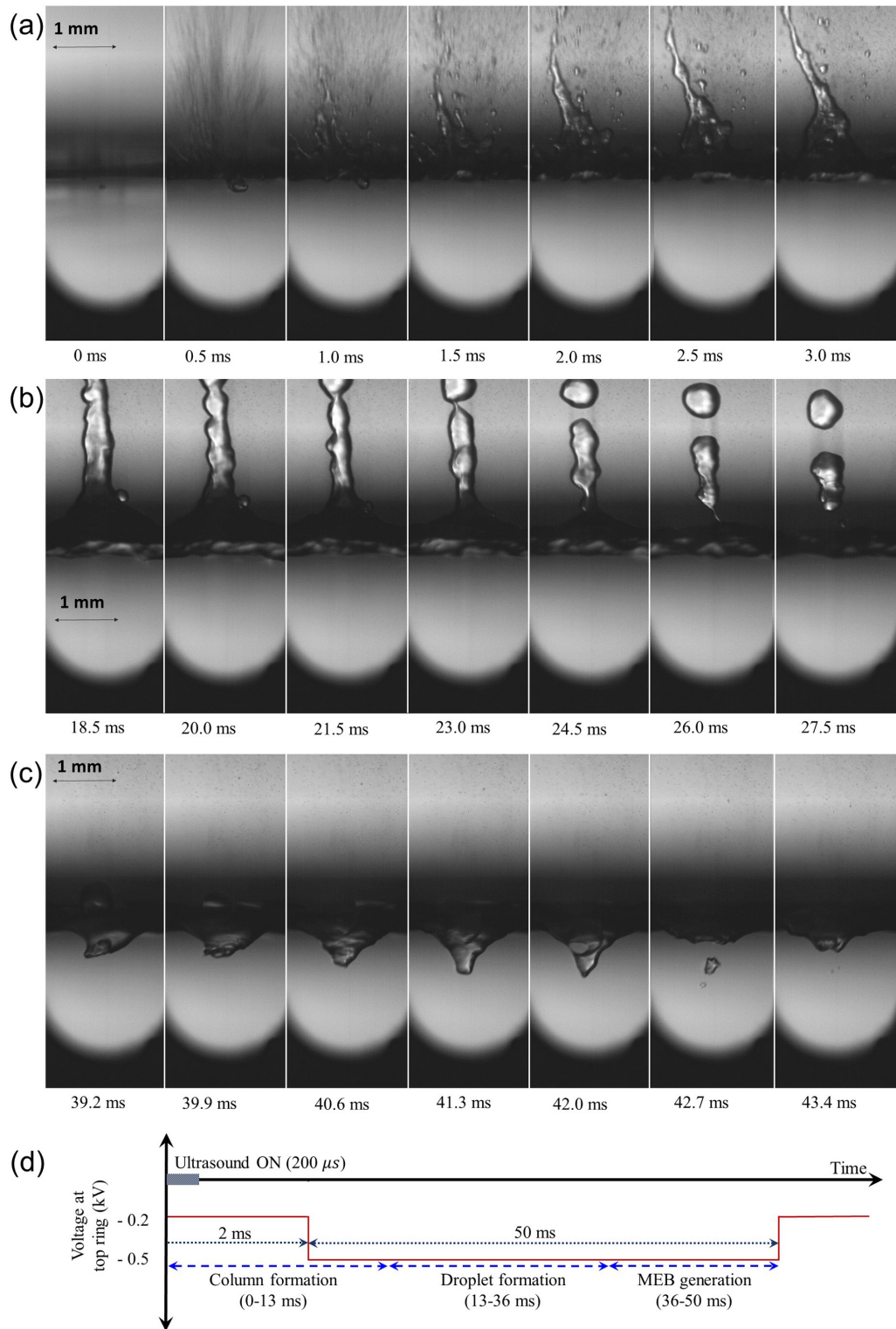
FIG. 2. Panel of images showing the creation of MEB assisted by the ultrasound. Panel (a) shows the effect of sound on the surface, resulting in the formation of droplets and subsequently, and formation of a liquid column (0–13 ms). Panel (b) shows the receding column along with formation of millimeter-size droplets (13–36 ms). Panel (c) shows the formation of MEBs as the droplets fall on the surface (36–44 ms); simultaneous negative voltage was applied to the top ring. Panel (d) shows the voltages applied at the top ring as a function of time (not to scale), checkered box represents the time for which ultrasound was ON.
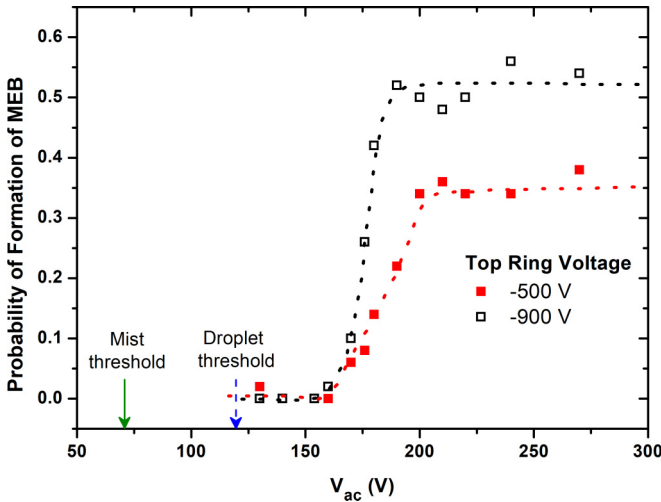
FIG. 3. Probability of MEB formation (out of 50 trials) as function of V_{ac} for two distinct top ring potential. Solid red squares and open black squares correspond to -500 and -900 V at the top ring. Dashed lines are guide to the eye. Note that the threshold in V_{ac} is independent of the top ring potential. The green and blue arrows correspond to the transducer voltages above which we could observe the formation of mist and droplets, respectively.

Fig. 3. We could detect a threshold V_{ac} for the formation of MEBs, which was independent of the top ring potential in the range of parameters shown here. We believe the threshold voltage $V_{ac} \sim 160$ V applied to the ultrasonic transducer corresponds to a minimum acoustic radiation pressure to form the liquid column, whose impact forms the MEBs. Also note that the arrows shown in Fig. 3(a) at $V_{ac} \sim 70$ V and $V_{ac} \sim 120$ V correspond to the transducer voltages at which we start observing the formation of mist (minimum detectable size $\sim 10\,\mu m$) and droplets, respectively. It is reasonable that at a slightly higher $V_{ac} \sim 160$ V, we should start observing the mechanical impact of the liquid column, made from coalescence of mist and droplets.

A similar thresholdlike behavior was also observed for the formation of ultrasonic-induced fog [18,19] in the past. When the helium surface was subjected to a vertical oscillation, a Faraday instability set in above a threshold acceleration; and if the drive was further increased, it reached a critical value for the Rayleigh-Taylor instability to set in. For our experiments, we also observed the thresholdlike behavior for the mist and droplet formation. The size of the droplet increases with the transducer drive, which in turn increases the probability of formation of MEBs.

As seen from the image corresponding to 39.2 ms in Fig. 2(c), the impact results in the formation of a large dimple on the liquid surface. Owing to its small curvature and the presence of pressing electric fields, the electrons accumulate inside the dimple, leading to a charge density that can trigger electrohydrodynamic instability of the surface. This picture was further confirmed through measurements of the probability of formation of MEBs as a function of top ring voltage for different V_{ac}. As shown in Fig. 4, irrespective of the mechanical impact signified by V_{ac}, the probability of MEB formation increased once the voltage applied to the top ring was more negative than ~ -300 V. This threshold corresponded to an
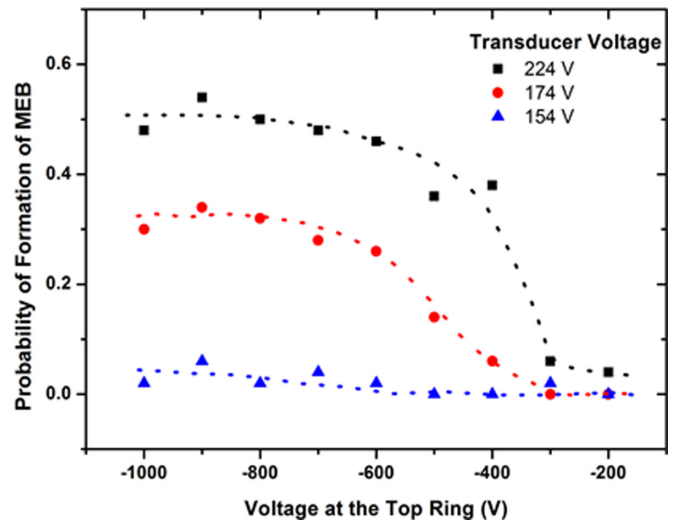

FIG. 4. Variation of the probability of MEB formation (out of 50 trials) as a function of potential at the top ring for different V_{ac}. Dashed lines are guides to the eye. The probability of bubble formation started to increase when the voltage was more negative than -300 V.

electric field $E_{expt} = 2.6$ kV/cm, as estimated from a finite element simulation (not shown). This value is smaller than the critical field ~ 4 kV/cm required for EHD of a flat liquid-vapor interface. As discussed in the next section, the critical ring voltage ~ 0.3 kV can be related to the probability of EHD due to the combined effect of the electric field and the mechanical induced deformation of the liquid surface.

IV. NUMERICAL SIMULATIONS

To estimate the charge distribution on the helium surface with and without a mechanically induced deformation, we performed numerical simulations. Due to the high mobility of free-surface electrons [20–23], the charges can redistribute on the surface with a time scale much shorter than that of the surface deformation, thus we assumed that at any given moment the charges are in electrical equilibrium, i.e., surface electrons are stationary. This implies that at any point on the surface, either the surface charge density is zero, or the tangential component of the electric field is.

The electric field experienced by electrons is the combination of field $\boldsymbol{E}_{ext}$ produced by applied voltages on various electrodes, and the field $\boldsymbol{E}_e$ produced by the surface electrons themselves. $\boldsymbol{E}_{ext}$ for the cell geometry under any voltage setting can be calculated relatively simply by finite difference methods, an example of which is shown in Fig. 5(a) (confinement ring at -500 V and top ring at -200 V). The calculation was performed on a rectangular grid of 0.1 mm spacing, with each boundary grid point set to its corresponding fixed voltage, and the Laplace equation $\nabla^2 V = 0$ is iteratively solved. Given the boundary voltages above, the electric field at the center of the helium surface is $\sim 3 \times 10^4$ V/m. We assumed that this part of the field is not affected by the electrons on the liquid surface, since even at saturation the electrons on the surface are much less numerous than the free charges on the electrodes. This is evidenced by the relative strength of
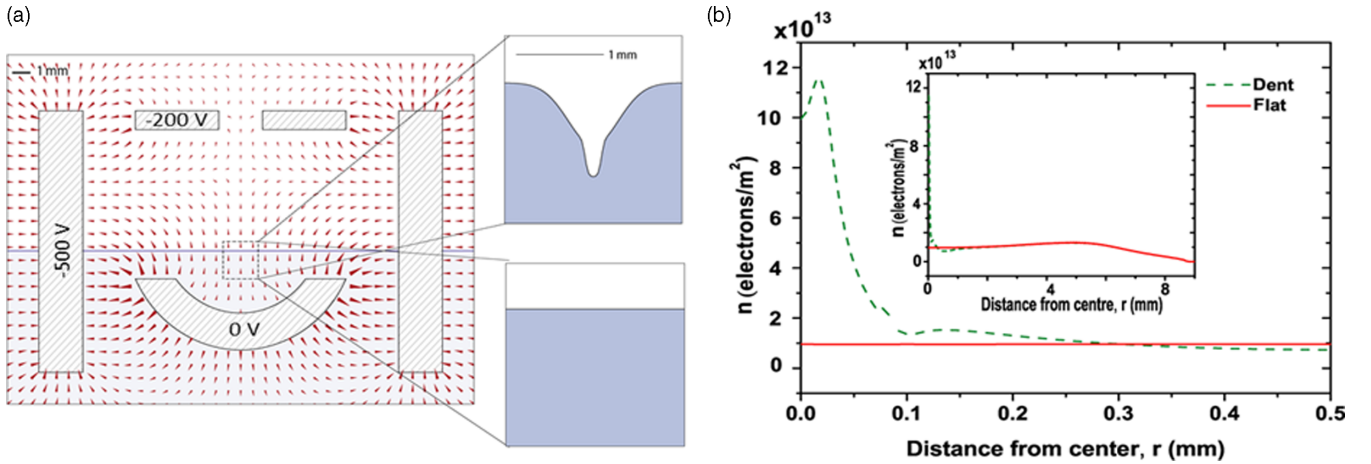
(a)

(b)

FIG. 5. (a) Arrow plot of the electric field in the system. The length of the arrow is proportional to the strength of the electric field. Also shown are the profiles of the surface in the center considered for calculating the surface charge density, flat and indentation. (b) Graph compares the surface charge density (*n*) for the two shapes of the surface, as calculated from the simulation. We can see that the charge density is increased significantly at the location of indentation. Inset shows the surface charged density over a longer distance.

field near the center of the surface vs that near the metals [see Fig. 5(a)], thus redistribution of electrons on the liquid surface should not significantly impact this external field. Calculating this external field is relatively straightforward; however, the interaction between the surface electrons E_e requires considerably more effort to compute.

Due to the near axial symmetry of the cell, we divided the liquid surface into some N concentric rings around the symmetry axis, each taken to have a uniform surface charge density, denoted ρ_i for the ith ring. Their positions are described in a spherical coordinate system whose origin is above the liquid surface at a distance comparable to the typical surface indentation size [$\sim$1 mm; see zoomed views in Fig. 5(a)]. It was done as such so that when the elevation angles θ_i are spaced uniformly, there are more rings near the region of interest (i.e., the center) to provide better spatial resolution of the charge distribution there (Fig. 6, left panel).

Each such electron ring generates a field E_i in space. Using the parameters as shown in Fig. 6 (right) with given line charge density ρ_i, the field is

$$E_i = \int_0^{2\pi} \frac{\rho_i R}{4\pi\epsilon_0} \frac{r\, d\phi}{r^3}$$

$$= \frac{\rho_i R}{4\pi\epsilon_0} \int_0^{2\pi} \frac{(\ell + R\cos\phi)\hat{x} + z\hat{z}}{\sqrt{z^2 + R^2 + \ell^2 + 2R\ell\cos\phi}^3} d\phi. \quad (3)$$

This is leads to an expression of complete elliptic integrals of the first and the third kind, for which efficient numerical methods are available [24]. From here we can calculate the equilibrium charge distribution in the form of ρ_i values satisfying the condition that all surface electrons see zero electric field tangential to the surface (see the Supplemental Material [25] for calculation of charge distribution).

For each voltage configuration, we first calculate the charge distribution of a flat surface at saturation in this manner to obtain the total charge. This same total charge is then used for the subsequent breaching of surface by the droplet, because the time scale of such an event is $\sim$1 ms, too short for the electron source to meaningfully add more electrons. Note the activity of the source is 15 mCi, and even if we assume 10% of the secondaries [26] enter the liquid, electrons are added to the liquid at a rate of 1.5×10^{11}/s. The surface indented by the droplet is empirically fitted to the function $z = -a_1 \exp[-(\frac{r}{\sigma_1})^2] - a_2 \exp[-(\frac{r}{\sigma_2})^4]$ with typical values of $\sigma_1 \sim 1$ mm and $\sigma_2 \sim 0.1$ mm. The first term corresponds to the broader base of the indentation, while the second corresponds to the narrower "tip" [compare Fig. 7(b) and schematic of Fig. 5(a)].

An example of the simulation result is in Fig. 5(b), with top ring voltage at -200 V and confinement cylinder at -500 V, and with the cell and every other electrode grounded. The maximum charge density on the flat surface came out to be $\sim 10^{13}$ electrons/m^2. This is expected, since higher electric

FIG. 6. Coordinate system as used in calculating electric field produced by surface electrons. Also shown (right) is the parameter for calculating field produced by an electron ring.
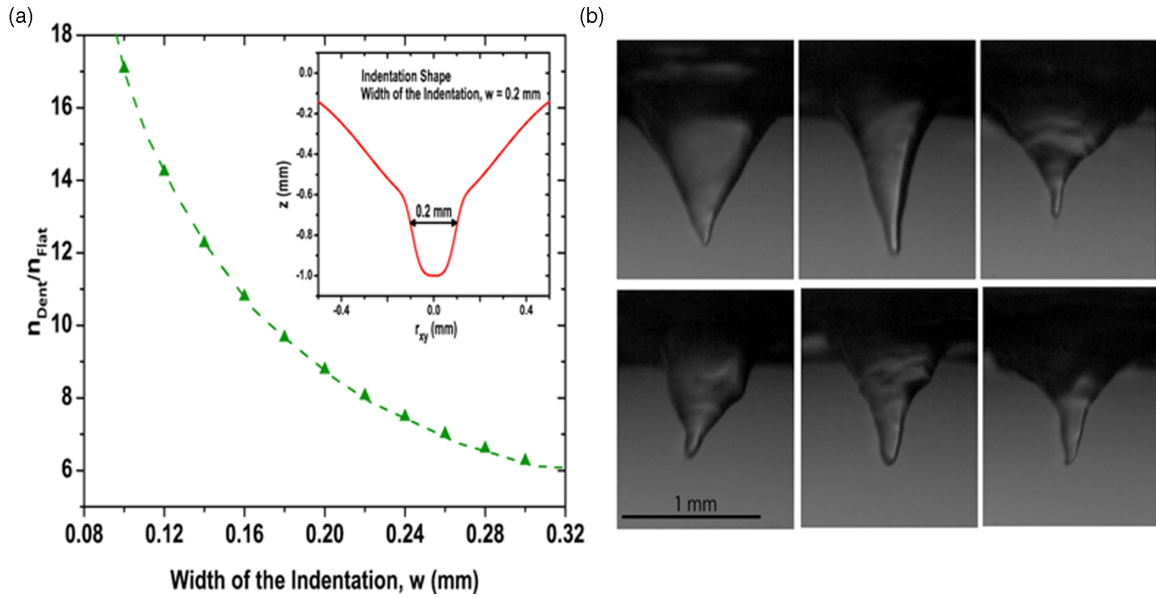
(a)

(b)

FIG. 7. (a) Plotted is the ratio of surface charge density of the indented surface and the plane surface vs the width of the indentation, as calculated from the simulation. An example of indentation has been plotted in the inset. The width of the indentation (w) is 0.2 mm. (b) Shown are some examples of experimentally seen indentations for different trials, recorded approximately 0.1 ms before the formation of MEBs.

fields resulted in electrohydrodynamic instability implied the surface was charged close to saturation. When the surface is breached by a droplet and an indentation forms [as in Fig. 7(a), top right], electrons concentrated into it, increasing the number density by about an order of magnitude. Note that the charge distribution away from the center is not significantly affected by the formation of the indentation [Fig. 5(b), inset], because the surface area of the dent is small compared to the entire liquid surface, thus only relatively few electrons need to move to fill it.

In Fig. 7(a), we have plotted the ratio of surface charge density of the indented surface and the flat surface ($n_{\mathrm{Dent}}/n_{\mathrm{Flat}}$)

as a function of the width of the indentation $w = 2\sigma_2$ (shown in the inset). This calculation was done assuming the surface charge density of the flat surface to be 1.3×10^{13} electrons/m^2 (where $n_c = 2 \times 10^{13}$ electrons/m^2). The maximum surface charge density increased as the width of the indent is made smaller, and the local charge density can reach well beyond the instability threshold to facilitate the breakup of the surface and thereby formation of multielectron bubbles. The widths were chosen in this range to be consistent with the experimental observations, as shown in Fig. 7(b).

It is important to note that indentation can influence the critical surface charge density for the development of
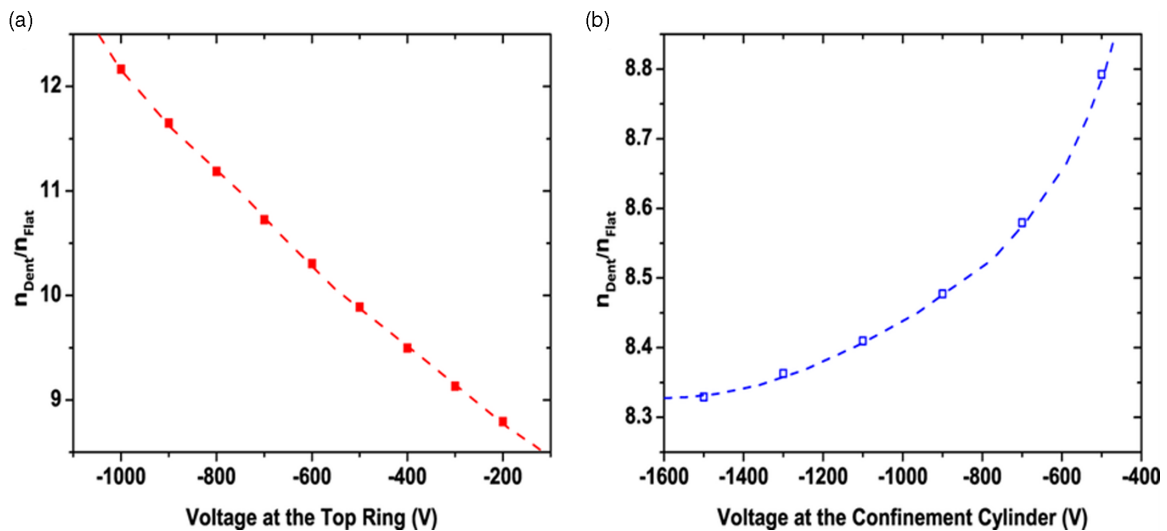
(a)

(b)

FIG. 8. (a) Plotted is the ratio of surface charge density of the indented surface and the plane surface vs the voltage at the top ring, as calculated from the simulation. As the voltage is varied, we see a significant change in the charge density, similar to what has been observed experimentally. (b) Plotted is the ratio of surface charge density of the indented surface and the plane surface vs the voltage applied at the confinement cylinder, as calculated from the simulation. The change in the charge density is not very significant.

EHD [27], given by $n_c(w) = (\frac{\alpha}{4e^2 w})^{1/2}$. For example, for $w = 0.2$ mm, the ratio of critical charge density of the indented surface to critical charge density of flat surface is approximately 1.5, implying a higher charge density is needed to create the EHD for smaller indentations.

We have also investigated the effect of electric field on the surface charge density. Figure 8(b) shows the n_{Dent}/n_{Flat} vs the voltage applied at the confinement cylinder. The corresponding number of charges is calculated for the given configuration and confinement cylinder voltage and hence the n_{Flat} and n_{Dent} for an indentation of width $w = 0.2$ mm are evaluated. The n_{Dent}/n_{Flat} do not vary much even when the confinement voltage is varied by a factor of 10. A similar exercise was performed for a fixed confinement voltage of -500 V and varying top ring potential. Figure 8(a) shows the result of n_{Dent}/n_{Flat} vs the top ring voltage. The variation of the top ring voltage leads to a more significant variation in n_{Dent}/n_{Flat}, implying the top ring potential will affect the probability of EHD and therefore generation of MEBs, in agreement with the experimental results shown in Fig. 4. Note that these calculations were performed assuming the charge on the flat surface rearranges itself when an indentation is formed in the surface without any loss of charge. However, some charge may get lost during the formation of the helium mist and column upon application of the ultrasound. Nevertheless, it

is interesting to note that the surface charge density can be increased by forming an indentation in the surface and by changing the top plate voltage, both of which are consistent with the experimental results.

V. DISCUSSION

The results shown in Figs. 2–4 correspond to experiments performed at 1.9 K. The vapor within the MEBs condense very quickly below the lambda point, resulting in a rapid reduction of the bubble size ($\sim$ a few ms for bubbles of initial size 100μm). We were limited by the imaging device in our experimental setup and were not able to detect MEBs smaller than 10μm. From Eq. (1) (with $P = 0$ and $\alpha = 3.09 \times 10^{-4}$ N/m), we conclude that the MEBs created in our experiments at 1.9 K contained fewer than 2.7×10^5 electrons.

To make a precise measurement of the number of electrons contained by the MEBs, we carried out the same experiments at 2.5 K, i.e., above the lambda point. Because of the reduced thermal transport of helium, the reduction of size is slower [11] (~ 1 s for a bubble size of 30μm) at these temperatures. For charge measurements at 2.5 K, after the creation of MEBs, a positive voltage was applied at the top ring to pull them back towards the surface, followed by a negative voltage to push them downward. Figure 9 shows snapshots
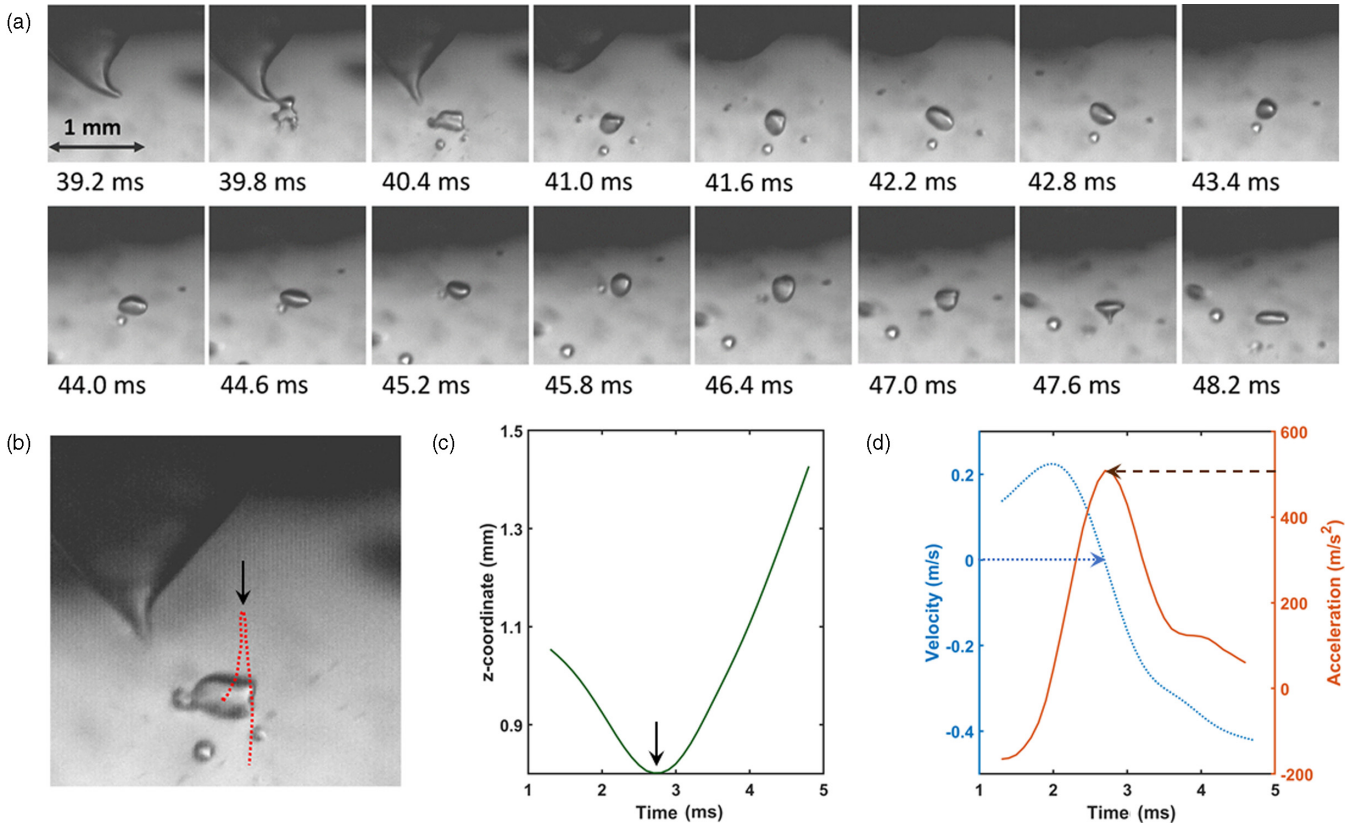

FIG. 9. (a) Formation of bubbles above lambda point (2.5 K) and response to change in electric field. In the initial frames the formation of MEBs can be seen. Direction of electric field was changed at 42 ms, by applying positive voltage at the top ring, MEBs reacted to the change and moved towards the plate. Field was again switched at 45 ms, by applying negative voltage at the top ring, and MEBs were pushed back into the liquid. (b) Trajectory of the bubble, (c) z coordinate as function of time. The turning point is marked with an arrow. (c) Velocity and acceleration estimated from the position of the MEB. We mark the turning point, at which the velocity becomes zero.

from this procedure. Following the methods outlined in our previous papers [11,16,17,28,29], at the turning point of the MEBs ($t \approx 45.5$ ms), where the vertical velocity is zero, this method allows for estimation of the charge without accurate knowledge of the hydrodynamic drag [30] experienced by the MEBs. We assume the bubbles are not affected by any convective flow, and the net force at the turning point can be written as a sum of the electrical and buoyant forces,

$$\boldsymbol{F}_{\text{net}} = \boldsymbol{F}_{\text{buoyant}} + \boldsymbol{F}_{\text{electric}}, \tag{4}$$

$$\tfrac{2}{3}\pi R^3 \rho \boldsymbol{a} = \tfrac{4}{3}\pi R^3 \rho \boldsymbol{g} + Ze\boldsymbol{E}. \tag{5}$$

Here $\boldsymbol{a}$ and $\boldsymbol{E}$ are the acceleration of the MEB and the electric field at the zero-velocity point respectively, from where we can estimate $Z = \frac{2(a-2g)\pi \rho R^3}{3eE}$. Typical trajectories, velocities, and acceleration of an MEB as a function of time has been shown in Figs. 9(c) and 9(d), where the turning points have been pointed out. Note that the electric field $\boldsymbol{E}$ was strongly dependent on the charge density of the liquid surface and therefore we estimated the electric field numerically (not shown) using a finite element simulation for two extreme cases: surface charged to saturation ($n_c = 2\times10^{13}$ electrons/m^2) and surface completely uncharged. This provides the maximum range of the number of electrons present inside an MEB of a certain radius, as shown by filled and empty circles in Fig. 10. Also shown with open triangles are results of measurements from a previous experiment [16], where the MEBs were created by confined field emission and the electric field was estimated by assuming an uncharged surface. The solid violet line shows the variation of radius vs charge for $n_p = 2\times10^{12}$ electrons/m^2, corresponding to the initial surface density of the MEBs typically seen in our previous experiments [16,28,29]. The blue solid line shows the theoretical value for the radius when the pressure is assumed to be zero inside the bubble. The green dotted line corresponds to a charge density of MEB equal to the saturation charge density (n_c). Clearly, for large bubble sizes, the bubbles created using ultrasound have very little to no vapor, unlike the ones created using confined field emission. We believe this was because heating of the surface was significant in confined field emission. We did not observe any collapse, as the typical time for collapse [11] of a 100-μm bubble is in the order of few seconds, much too long compared to our measurement duration 50–100 ms.

We also show in Fig. 10 the radius vs charge for $n_1 = 9\times10^{13}$ electrons/m^2 and $n_2 = 4.5\times10^{14}$ electrons/m^2 in the dotted blue line and dashed green line respectively. At these densities n_1 and n_2, the Fermi energy of a flat 2DES equals 10% and 50% of the thermal energy at 2.5 K, implying significant quantum correlations. We recognize this estimate would need to be corrected for curved surfaces [3,31–33], however, the crucial point to note is that 2DES inside MEBs created in our experiments may have strong quantum fluctuations even before all the vapor has condensed, and these MEBs can be simultaneously imaged. Densities for some MEBs in our experiments, once the vapor condenses, are expected to be higher than the maximum density [10] achieved with electrons on charged thin films, however, one must note that the Coulomb interaction and therefore phase diagram of
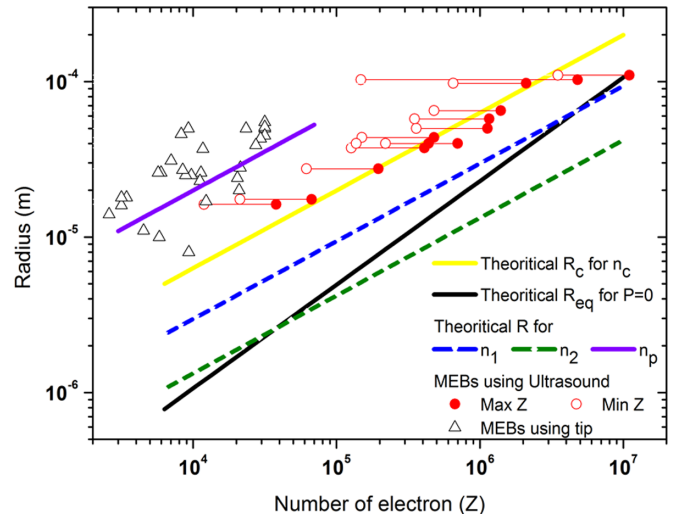

FIG. 10. Radius of the MEBs plotted as function of number of electrons. MEBs created using field-emission tip [16] are shown by open black triangles; here the analysis assumed that the surface was free of charges. We assumed the surface tension to be 2.62×10^{-4} N/m, corresponding to temperature 2.5 K. Solid red circles show the maximum charge (uncharged surface) and open red circles show the minimum charge (charged surface) of MEBs created with ultrasound assistance. Solid black line shows the theoretically predicted radius when pressure inside is zero, given by Eq. (2). Solid yellow line is the theoretically predicted radius [$R_c = (Z/4\pi n_c)^{1/2}$] when the number of electrons inside it is equal to the critical number density ($n_c = 2\times10^{13}$ electrons/m^2) of electrons for EHD to set in for bulk surface. Solid violet line shows the variation of radius vs charge for $n_p = 2\times10^{12}$ electrons/m^2, corresponding to the initial surface density of the MEBs typically seen in our previous experiments [16,28,29]. Dotted blue and green lines show the radius vs charge for $n_1 = 9\times10^{13}$ electrons/m^2 and $n_2 = 4.5\times10^{14}$ electrons/m^2, corresponding to densities where the thermal energy at 2.5 K equals 10% and 50% of the Fermi energy of a flat 2DES of same density ($\frac{E_F}{k_BT} = 0.1$ and $\frac{E_F}{k_BT} = 0.5$).

the electrons on thin films is significantly modified by the dielectric constant of the substrate [7], unlike electrons within MEBs. It would be extremely interesting in the future to create MEBs using this technique and subsequently cool down to lower temperatures to have reduced thermal fluctuations, so as to have a 2D electron solid with strong quantum correlations. As far as we know, such a phase is yet to be achieved in the absence of magnetic field in any experimental system [6], be it 2DES above helium or semiconductor-based solid-state experimental systems.

In all the analysis, we assumed the bubbles to be in stationary bulk liquid far away from all boundaries and also neglected any possible contribution from history forces [34–39]. Including the history force can only modify the charge of an MEB by a factor of 2–3 (see the Supplemental Material [25] for more details), which does not alter the main messages presented here.

To revisit the experiments below the lambda point, if the number density during generation were as high as n_c, the size of a bubble when all the vapor condenses should be close to $10\,\mu$m. This was large enough to be detected in our setup but
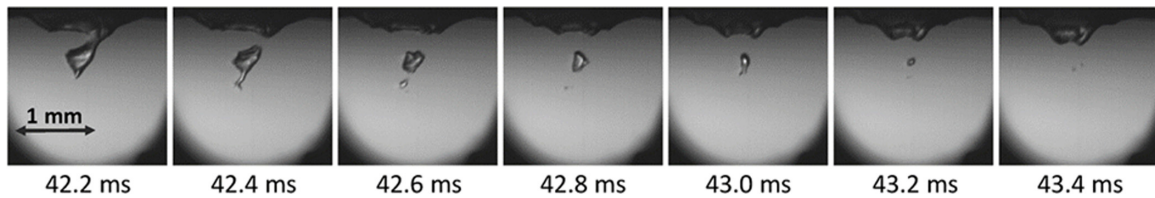
FIG. 11. Formation of MEBs below lambda point; this is the same MEB as seen in Fig. 1. At $t = 42.2$ ms, MEB is about to be ejected out of the surface. In the subsequent frames, the big MEB breaks into smaller bubbles finally reducing in size, after which it becomes smaller than the resolution of imaging setup.

was never observed. As shown in Fig. 11, after the formation of the MEB, it ejects smaller MEBs ($t = 42.4$ ms), possibly sharing the charge between the daughter bubbles [29]. It is further seen that at $t = 42.8$ ms the smaller MEB again breaks into two and disappears. This instability can be attributed to the highly deformed structure of the MEB and has been observed in the past [40].

VI. CONCLUSIONS

We report a method of generation of MEBs using low electric fields and ultrasound-induced mechanical deformation of the charged surface of liquid helium. We measured the dependence of the formation of MEBs on the acoustic pulse width, as well as electric fields applied across the interface. A numerical simulation supports the hypothesis that an indentation is formed on the charged surface through mechanical impact, and this can lead to a significant increase in the local surface charge density and thereby the generation of MEBs. It may be possible to generate the mechanical indentation

using other means as well, for example through externally controlled moving mechanical parts near the charged liquid surface. Compared to MEBs generated before using confined field emission, the MEBs reported here had significantly higher initial surface charge density and therefore may be observable even after the vapor condenses. We expect the 2DES within these MEBs to have strong quantum correlations, which may influence the shape oscillations of the bubbles and thus be detected through direct optical imaging. There would be additional interesting effects arising due to electrons being pushed into nanoscale dimples on the bubble surface through Coulomb repulsion, providing a platform for simultaneous investigation [41] of the role of curvature and quantum interactions in this system of interacting electrons.

[1] W. T. Sommer, Phys. Rev. Lett. **12**, 271 (1964).

[2] A. P. Volodin, M. S. Khaikin, and V. S. Edel'man, Pis'ma Zh. Eksp. Teor. Fiz. **26**, 707 (1977).

[3] J. Tempere, I. F. Silvera, and J. T. Devreese, Surf. Sci. Rep. **62**, 159 (2007).

[4] P. Leiderer, J. Low Temp. Phys. **87**, 247 (1992).

[5] N. Yadav, P. K. Rath, Z. Xie, Y. Huang, and A. Ghosh, J. Low Temp. Phys. (2020).

[6] T. Ando, A. B. Fowler, and F. Stern, Rev. Mod. Phys. **54**, 437 (1982).

[7] F. M. Peeters and P. M. Platzman, Phys. Rev. Lett. **50**, 2021 (1983).

[8] J. Angrik, A. Faustein, J. Klier, and P. Leiderer, J. Low Temp. Phys. **137**, 335 (2004).

[9] P. Leiderer, E. Scheer, K. Kono, J. Lin, and D. G. Rees, J. Low Temp. Phys. **183**, 258 (2016).

[10] T. Günzler, B. Bitnar, G. Mistura, S. Neser, and P. Leiderer, Surf. Sci. **361-362**, 831 (1996).

[11] A. Pal, E. Joseph, V. Vadakkumbatt, N. Yadav, V. Srinivasan, H. J. Maris, and A. Ghosh, J. Low Temp. Phys. **188**, 101 (2017).

[12] W. Guo, D. Jin, and H. J. Maris, Phys. Rev. B **78**, 014511 (2008).

[13] J. Tempere, I. F. Silvera, and J. T. Devreese, Phys. Rev. B **67**, 035402 (2003).

[14] J. Fang, J. Tempere, and I. F. Silvera, J. Low Temp. Phys. **187**, 54 (2017).

[15] U. Albrecht and P. Leiderer, Europhys. Lett. (1987).

[16] V. Vadakkumbatt, E. Joseph, A. Pal, and A. Ghosh, Nat. Commun. **5**, 4571 (2014).

[17] E. M. Joseph, V. Vadakkumbatt, A. Pal, and A. Ghosh, J. Low Temp. Phys. **187**, 580 (2017).

[18] H. Kim, K. Seo, B. Tabbert, and G. A. Williams, Europhys. Lett. **58**, 395 (2002).

[19] H. Kim, K. Seo, B. Tabbert, and G. A. Williams, J. Low Temp. Phys. **121**, 621 (2000).

[20] W. T. Sommer and D. J. Tanner, Phys. Rev. Lett. **27**, 1345 (1971).

[21] A. S. Rybalko, Y. Z. Kovdrya, and B. N. Esel'son, Pis'ma Zh. Eksp. Teor. Fiz. **22**, 569 (1975).

[22] R. Mehrotra, C. J. Guo, Y. Z. Ruan, D. B. Mast, and A. J. Dahm, Phys. Rev. B **29**, 5239 (1984).

[23] C. C. Grimes and G. Adams, Phys. Rev. Lett. **36**, 145 (1976).

[24] B. Carlson, Digit. Libr. Math. Funct. Online at https://dlmf.nist.gov/19 (n.d.).

[25] See Supplemental Material at http://link.aps.org/supplemental/10.1103/PhysRevB.102.054509 for calculation of charge distribution and effect of history force on estimation of charge.

[26] G. M. Seidel, T. M. Ito, A. Ghosh, and B. Sethumadhavan, Phys. Rev. C **89**, 025808 (2014).

[27] D. Marty, J. Phys. C: Solid State Phys. **19**, 6097 (1986).

[28] V. Vadakkumbatt and A. Ghosh, in J. Phys.: Conf. Ser. **969**, 012018 (2018).

[29] V. Vadakkumbatt and A. Ghosh, J. Low Temp. Phys. **187**, 369 (2017).

[30] U. Albrecht and P. Leiderer, J. Low Temp. Phys. **86**, 131 (1992).

[31] M. M. Salomaa and G. A. Williams, Phys. Rev. Lett. **47**, 1730 (1981).

[32] M. M. Salomaa and G. A. Williams, Phys. Scr. **T4**, 204 (1983).

[33] J. Tempere, I. F. Silvera, and J. T. Devreese, Phys. Rev. B **65**, 195418 (2002).

[34] H. J. Maris, Am. J. Phys. **87**, 643 (2019).

[35] A. Basset, *A Treatise on Hydrodynamics: With Numerous Examples* (Deighton, Bell and Co, Cambridge, 1888).

[36] J. V. Boussinesq, CR Hebd. Seanc. Acad. Sci. Paris **100**, 935 (1885).

[37] I. Kim, S. Elghobashi, and W. A. Sirignano, J. Fluid Mech. **367**, 221 (1998).

[38] M. R. Maxey and J. J. Riley, Phys. Fluids **26**, 883 (1983).

[39] P. M. Lovalenti and J. F. Brady, J. Fluid Mech. **256**, 561 (1993).

[40] E. M. Joseph, V. Vadakkumbatt, A. Pal, and A. Ghosh, J. Low Temp. Phys. **175**, 78 (2014).

[41] J. Tempere, S. N. Klimin, I. F. Silvera, and J. T. Devreese, Eur. Phys. J. B **32**, 329 (2003).